Journal of Biomechanics 97 (2019) 109434

Contents lists available at ScienceDirect

Journal of Biomechanics

journal homepage: www.elsevier.com/locate/jbiomech
www.JBiomech.com

Review

In silico approaches to respiratory nasal flows: A review

Kiao Inthavong [a], Prashant Das [b], Narinder Singh [c], Josué Sznitman [d]

[a] School of Engineering, RMIT University, Australia
[b] Department of Mechanical Engineering, University of Alberta, Edmonton, Canada
[c] Dept of Otolaryngology, Head & Neck Surgery, Westmead Hospital Clinical School, Faculty of Medicine, University of Sydney, Australia
[d] Department of Biomedical Engineering, Technion – Israel Institute of Technology, Haifa, Israel

ARTICLE INFO

Article history:
Accepted 17 October 2019

Keywords:
Nasal airflow
CFD
Nose
Fluid dynamics

ABSTRACT

The engineering discipline of *in silico* fluid dynamics delivers quantitative information on airflow behaviour in the nasal regions with unprecedented detail, often beyond the reach of traditional experiments. The ability to provide visualisation and analysis of flow properties such as velocity and pressure fields, as well as wall shear stress, dynamically during the respiratory cycle may give significant insight to clinicians. Yet, there remains ongoing challenges to advance the state-of-the-art further, including for example the lack of comprehensive CFD modelling on varied cohorts of patients. The present article embodies a review of previous and current *in silico* approaches to simulating nasal airflows. The review discusses specific modelling techniques required to accommodate physiologically- and clinically-relevant findings. It also provides a critical summary of the reported results in the literature followed by an outlook on the challenges and topics anticipated to drive research into the future.

Contents

E-mail address: kiao.inthavong@rmit.edu.au (K. Inthavong)

https://doi.org/10.1016/j.jbiomech.2019.109434

1. Introduction

Over the past decades, *in silico* computational modelling of nasal flows has steadily increased. The recent advancement of this discipline is attributed to availability of Computational Fluid Dynamics (CFD), and advances in computer science and clinical imaging modalities. Among the earliest computational studies of airflow through a human nasal cavity are Elad et al. (1993), and Keyhani et al. (1995). From these two works, the number of computational studies, and the modelling complexity therein, has consistently grown owing primarily to faster and more powerful computing resources.

A comprehensive survey of *in silico* studies on nasal flows between 1993 and 2018 was performed. The survey searched the keywords 'nasal CFD' using the internet search engine 'Google Scholar'. The search results were evaluated to determine if a publication addressed any aspect of fluid flow in human nasal cavities using *in silico* techniques. Typically, this meant reviewing approximately 200 publications for each year. Fig. 1 shows the number of articles (of relevance to this review) published annually between 1993 and 2018. It is worth noting that between 2004 and 2009, there was a surge in the number of articles published, with continued growth up until the present culminating in nearly 80 related publications in both 2017 and 2018. As a correlation, a search using SCOPUS database (Web of Science) was performed using the keywords 'nasal' AND 'Computational Fluid Dynamics' and the results were directly used without any scrutiny.

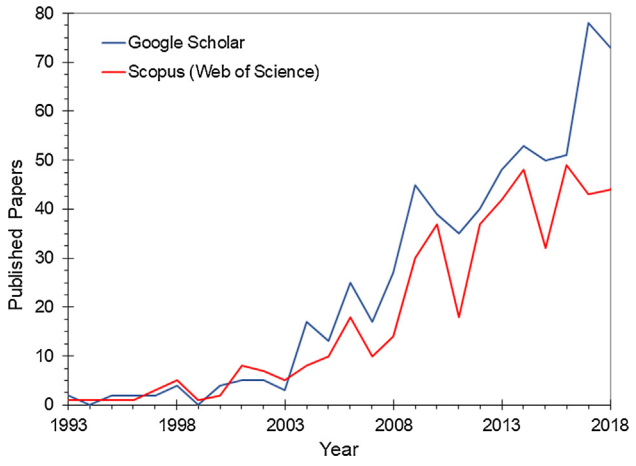

Fig. 1. Number of published articles of relevance to the computational modelling of fluid dynamics in the human nasal cavities, as obtained in the literature using the keyword search *nasal CFD* in Google Scholar database, and *nasal* AND *Computational Fluid Dynamics* in SCOPUS (Web of Science) database.

This review summarizes past and current progress in the field beginning with CFD modelling techniques. This is followed by a discussion of the physiologically- and clinically-relevant findings arising from the computational modelling. In particular, the results follow the journey along the inhaled flow from the entrance of the nostrils, through to the nasopharynx. The review culminates with a discussion on anticipated future progress and applications.

2. Creating the computational model

2.1. Airway reconstruction

2.1.1. Image acquisition

Airway geometry data are typically obtained through medical images acquired from computed tomography (CT) or magnetic resonance imaging (MRI). Although non-invasive, CT scans send X-ray beams through the body and therefore ionizing radiation exposure is a concern. MRI uses magnetic fields and radio frequency pulses to produce images, and does not suffer from the limitations of ionizing radiation exposure. While MRI distinguishes mucosal structures well, the nasal turbinate bone location often needs to be inferred from its surrounding mucosa, since actual bone structures appear dark (low-signal) on MRI scans and may not be visible (see Fig. 2). The predominance of air in the nasal cavity, and the long scan time makes MRI susceptible to low signal-to-noise ratio during the respiration cycle where the airway geometry changes with time.

Recently four-dimensional computed tomography (4D-CT), was used where a moving structure is imaged over a period of time (Kwong et al., 2015; Miyawaki et al., 2016), while four-dimensional magnetic resonance imaging (4D-MRI) has also emerged (Cai et al., 2011). Long-range optical coherence

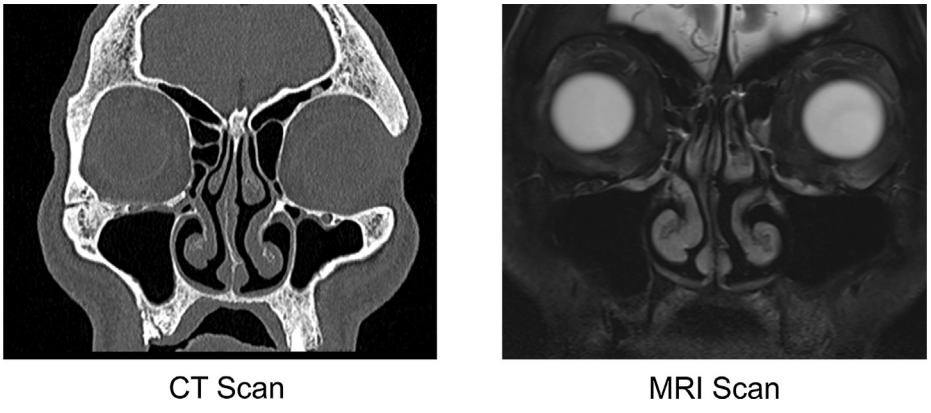

Fig. 2. Example of the typical image contrast obtained from (a) CT and (b) MRI modalities. The scans are coronal planes of the main nasal passage at the level of the maxillary sinuses. CT scans provide sharp contrast at the nasal airway-wall interface, while the MR scans show darker greyscale values for the cartilage, and bone, making segmentation more challenging.

tomography (LR-OCT) is another technique that provides an outline of the airway, buts it is yet to be applied to imaging nasal cavities.

2.1.2. Segmentation

Reconstruction of the nasal passages involves image segmentation, which is the partitioning of scanned images into a number of homogeneous segments, such that any two neighbouring segments yield a heterogeneous segment. Some common algorithms include thresholding, edge detection, and region characteristics (Pal and Pal, 1993; Zhang, 2001). Automated segmentations have been developed where Neelapu et al. (2017) and Bui et al. (2015) presented an automatic segmentation algorithm to segment pharyngeal- and sino-nasal airway sub-regions on 3D-CT imaging datasets. Cercos-Pita et al. (2018) released an open-source tool, i.e. NASAL-Geom, consisting of an automated 3D segmentation tool. Similarly, Burgos et al. (2017) integrated a segmentation technique into a software package with CFD analysis tool for rhinologists. While the segmentation is automated, there is a reliance on the scan quality, and pre-processing the data files to ensure the automated segmentation produces the correct volume of interest.

Some accuracy issues include image slice thickness where 1 mm or less provides good contrast for defining airway boundaries, but increases radiation exposure and image noise in CT. Postural position is known to affect nasal patency (Zubair et al., 2013b; Roithmann et al., 2005), where Kase et al. (1994) found a decrease in airway dimension of about 16% in 8 young adult subjects 6 min after changing from seated to supine position. Patient movement can also be a factor to consider in MRI scans as these require approximately 10 min of continuous acquisition.

Physiological variations involve the health and state of the nasal cavity at the time of scan; this is mostly influenced by congestion and nasal cycling. The nasal cycle represents a periodic, alternating, asymetric congestion and decongestion of each nasal chamber. As a result, reconstructed computational models often depict asymmetric volumes between the left and right nasal chambers. Inthavong et al. (2017) reported six nasal cavity volumes which showed a mean of 10.8 cm^3 with asymmetric distribution between nasal chambers of 45% and 55%, respectively. To avoid this asymmetry, many researchers routinely have test subjects use nasal decongestants prior to scanning (Negley et al., 1999; Adil et al., 2012; Corey et al., 1997). While this avoids cyclic asymmetry, it does result in a nasal cavity volume that is larger than the physiological norm.

Subjective variations arise from an operator's decision-making process of defining the nasal wall boundaries. Scans with thick slices produce successive slices that need to be connected by interpolation using, for example, cubic splines, followed by a smoothing process. Doorly et al. (2008) highlighted that smoothing steps result in volume shrinkage, especially in regions of high curvature that are commonplace within the nasal passages.

2.2. CFD and mesh independence

The segmented airway is converted into a geometric model which is then meshed. Typically, a larger number of mesh elements in the model translates to smaller scales of flow that can be resolved. An indication of how the number of mesh elements has increased over the last three decades is shown in Fig. 3 (obtained from the literature survey). The early studies of Elad et al. (1993) used just under 10,000 mesh elements and Keyhani et al. (1995) used approximately 77,000 mesh elements. In general, early studies (prior to 2003) typically used less than 1 million elements, while this increased up to as high as 44 million elements by Calmet et al. (2016). The large variations in mesh numbers among different studies has led to investigations of what constitutes a sufficient mesh. Vinchurkar and Longest (2008), Frank-Ito et al. (2015), and most recently Bass and Worth Longest (2018) recommended the use of hybrid tetrahedral-prism meshes to resolve the near wall boundary layers, with Frank-Ito et al. (2015) suggesting the use of 4 million tetrahedral cells with three prism layers (for near wall resolution), in line with studies by Schroeter et al. (2011), Shang et al. (2017), and Tong et al. (2016).

The optimum number of mesh elements to be used depends on the flow variable to be predicted, for example with integrated pressure loss less demanding than regional wall shear stress

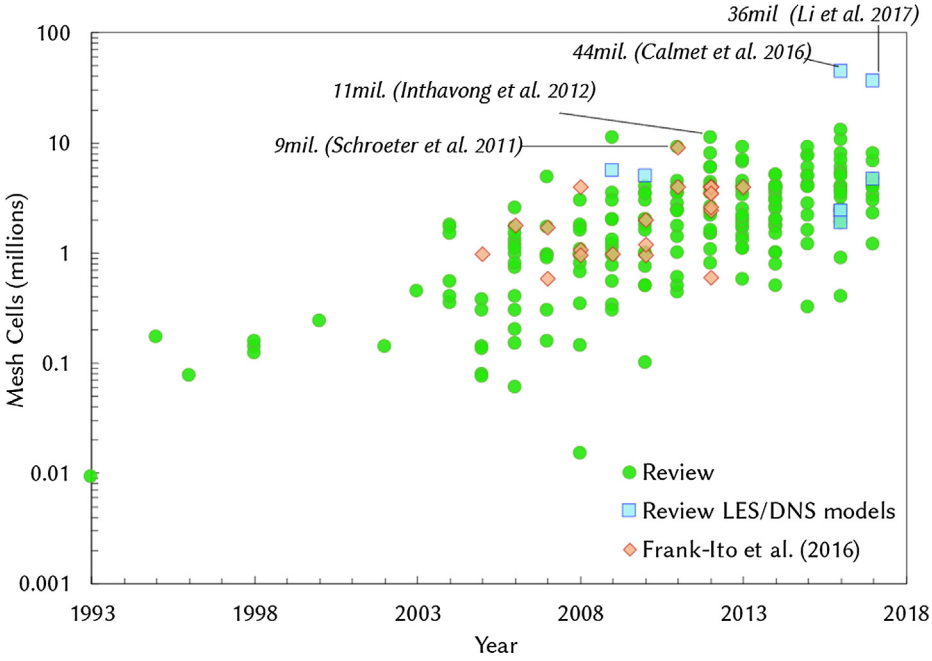

Fig. 3. Number of mesh cell elements reported in the literature in the period between 1993 and 2017. Examples of some high meshed nasal models are highlighted (e.g. Inthavong et al. 2012; Schroeter et al., 2011). The studies with very large number of cells (e.g. Calmet et al. 2016; Li et al. 2017) are linked to high-fidelity turbulent flow modeling using Large Eddy Simulations (LES) or Direct Numerical Simulations (DNS).

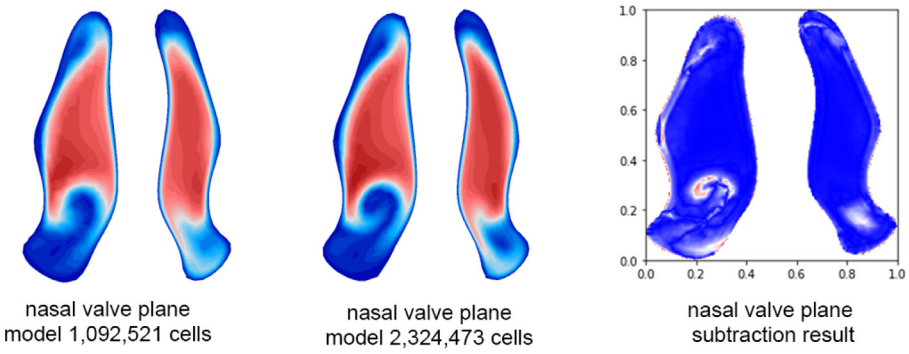

(a) Subtraction along 2D planes of velocity fields taken from a nasal cavity model at the nasal valve.

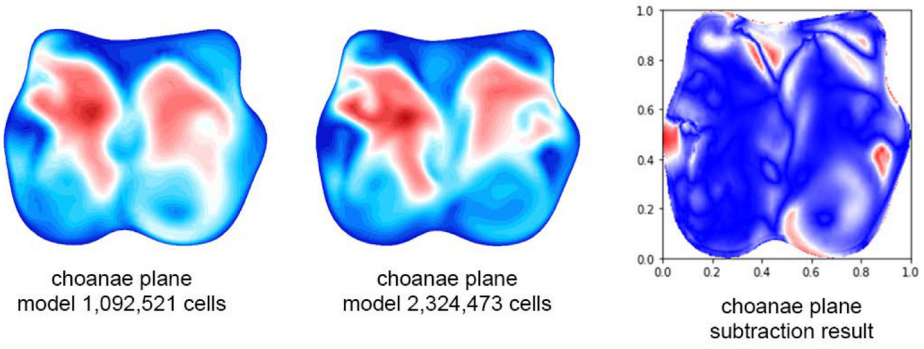

(b) Plane subtraction taken from a nasal cavity model at the choanae valve.

Fig. 4. Plane subtraction of velocity fields between nasal cavity models with 1-million and 2-million cells. The subtracted results shows large differences (red) versus little or none (blue). Reproduced from Inthavong et al. (2018). (For interpretation of the references to colour in this figure legend, the reader is referred to the web version of this article.)

distribution. In each case it can be determined by a mesh independence study, i.e. when the results from a simulation do not vary significantly with successive mesh refinements. Estimates of the discretization error may be performed by Richardson extrapolation (Richardson, 1910), although such estimates can be quite inaccurate if not applied carefully. More recently, the Grid Convergence Index (GCI) was introduced by Roache (1994) as a method for uniform reporting of CFD results.

A simpler method widely adopted is plotting a flow variable against the number of cells and comparing its trend over successively refined models. This could be in the form of a local parameter such as velocity along a selected line profile (Inthavong et al., 2008). A drawback to this method, however, is that specific line locations are arbitrary and it only characterizes local mesh independence. This is unsuitable for representing the entire flow domain. Alternatively, an averaged global parameter such as pressure drop or averaged wall shear stress across the entire domain may also used (King Se et al., 2010). However, this global evaluation can mask local regions that have large flow gradients and may not be sufficiently resolved.

An alternative is to use a 2D cross-sectional plane subtraction method, where scalar values (e.g. velocity magnitude) from a cross-sectional plane are interpolated onto a regularly spaced grid. The interpolated grid values from any two meshed models can then be compared through subtraction. (see Fig. 4). Details of this method are given in Inthavong et al. (2018) where it was found that 6 planes across the nasal cavity were suitable for representing the entire domain. An extension to 3D volume subtraction was also proposed. The method quantified incremental changes for each successive refined mesh, and found the posterior choanae was the last region to reach mesh convergence. This suggests mesh refinements can be targeted locally thereby reducing the number of cells, when compared to performing global mesh refinement.

2.3. Influence of meshing on CFD solutions

In the following discussion, we limit ourselves to meshing of the Finite Volume Method because of its widespread prevalence in CFD simulations of the nasal cavities since its adoption by major commercial software (e.g. Ansys-Fluent, Ansys-CFX, Star-CCM), and by OpenFoam® (a major open source software). Unstructured tetrahedral cells are widely used for mesh generation since they allow maximum flexibility in fitting to the complex nasal cavity geometry (Shi et al., 2006; Schroeter et al., 2011; Calmet et al., 2016; Goodarzi-Ardakani et al., 2016). However, such cells are prone to high aspect ratios that affect the cell skewness, leading to poor solution convergence and at worst, solution divergence. Additionally, cells are not guaranteed to align with the flow direction leading to false numerical diffusion. Increasing the mesh resolution can fix skewed cells, while higher order discretization schemes can minimize the likelihood of false diffusion (Anderson, 1995; Fletcher, 2013; Tu et al., 2012).

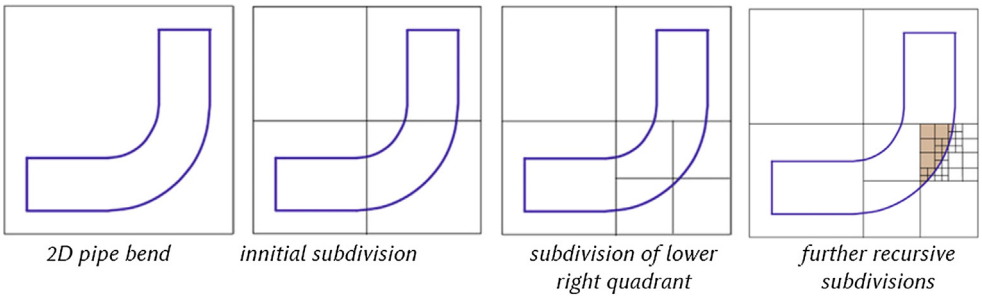

(a) example of quadtree/octree subdivisions, e.g. cut-cell cartesian meshing

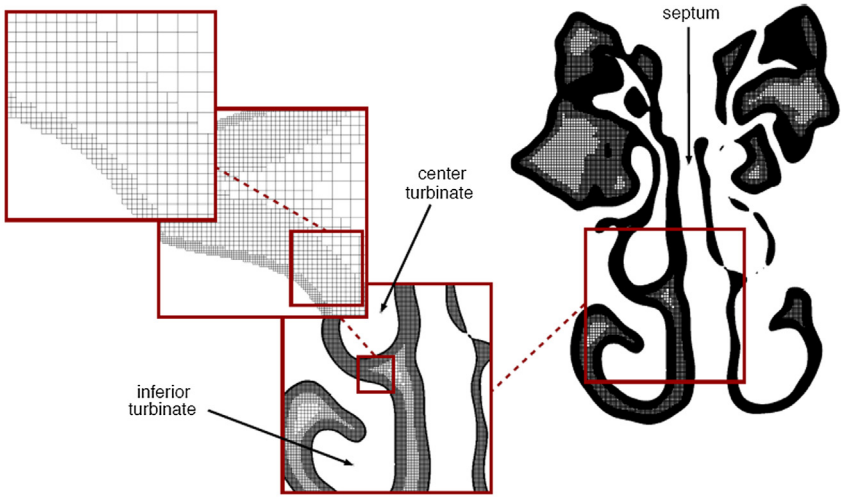

(b) Unstructured grid with 1.8 x10⁹ cells - image taken from Lintermann and Schroder (2017)

Fig. 5. (a) A quadtree subdivision concentrating only on the bottom right corner region. A criterion of whether a region is filled by the interior of the 90° bend is used. During subdivision, a region that is outside of the domain is neglected. (b) Cartesian meshing from Lintermann and Schröder (2017).

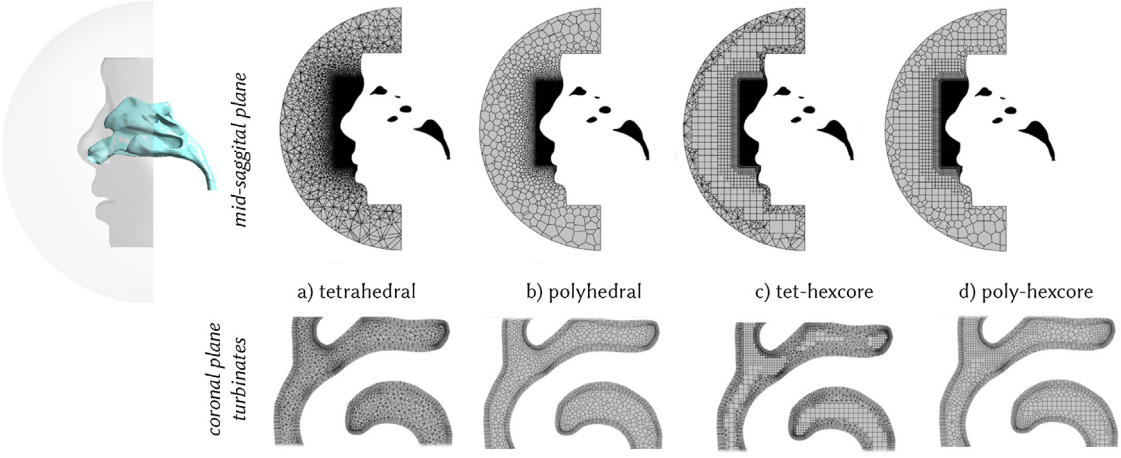

Fig. 6. Hybrid mesh types using prism layers plus (a) tetrahedral; (b) polyhedral; and combinations of (c) tetrahedral with hexahedral-core (d) polyhedral with hexahedral-core.

Unstructured mesh elements are also ineffective in resolving wall-boundary layers since tetrahedrals do not deform (i.e. stretch or bend) during local refinement to make cells very small. Instead, prism layers are used to resolve the near-wall boundary layers (Frank-Ito et al., 2015; Vinchurkar and Longest, 2008; Zubair et al., 2013a). One error that arises with prism layers is the presence of high-aspect ratio cells. When this exists round-off errors evolve from the conservation properties of the equations (large differences in flow length scales or large variations in flow variables also contribute). In such cases double-precision numbers should be used

to minimize possible round-off errors from perpetuating (Anderson, 1995; Fletcher, 2013; Tu et al., 2012); however, whether a simulation uses single or double precision is rarely reported in the literature.

Structured mesh elements are essentially rectangular or hexahedral cells, where flow conservation properties are easily defined because each face must have four nodes and four lines. Thus, a pair of inlet/outlet fluxes can be defined on the six faces of a cube. These grids are also referred to as Cartesian grids as they maintain their *x*-*y*-*z* (or *i*-*j*-*k*) mesh index notation. To overcome the challenge of fitting the curvilinear nasal cavity geometry within Cartesian grids, a quadtree/octree subdivision method is used. This is also called a 'cutcell' method or the divide-and-conquer principle, illustrated by Tucker and Pan (2000). As an outcome, a staircase jagged shape is produced around the curvilinear boundaries, however, very fine mesh elements can be used to minimize this effect.

Examples of cartesian meshing include the work by Lintermann and Schröder (2017) (on a nose-like model, see Fig. 5) and Kimura et al. (2019), although the CFD approaches used were not Finite Volume Method but rather a Voxel-based simulation and Lattice Boltzman Method, respectively. Recently there has been rapid adoption of polyhedral (and poly-hexcore) cells to fill the interior domain (Dong et al., 2018a; Bates et al., 2017; Inthavong et al., 2017; Tian et al., 2017). It allows the flexibility of an unstructured mesh to be applied to a complex geometry with improved mesh skewness. Typically, a smaller number of mesh elements is used and faster convergence is obtained when compared to tetrahedral cells. Fig. 6 illustrates the different meshes possible.

3. Modelling nasal airflows

3.1. Existence of laminar and turbulent flows

In smooth regular pipes, the onset of turbulence is identified by the Reynolds number, $\mathrm{Re} = \rho U D_h/\mu$ where ρ is density, U is velocity, D_h is hydraulic diameter, and μ is dynamic viscosity. Studies have defined the hydraulic diameter D_h as either the nostril inlet (Inthavong et al., 2008; Subramaniam et al., 1998), or the internal nasal valve (Taylor et al., 2009; Calmet et al., 2016). The nasal geometry consists of irregular cross-sections, 90°-like bends at the nasal vestibule and nasopharynx, converging and diverging sections, and mixing flows - all contributing to flow disturbances. Therefore, the Reynolds number criteria based on regular smooth pipe flows is unreliable for identifying the onset of turbulence, but perhaps more useful as a reference.

Flow in the nasal cavity is most likely to experiences both laminar and turbulent regimes. Doorly et al. (2008) stated that transition from laminar to turbulence is unclear in nasal flows, and flows may actually never become fully turbulent, nor are they ever fully laminar; rather they constitute a disturbed laminar flow. Experimental measurements from Hahn et al. (1993) showed that at a flow rate of 180 mL/s through a single nasal chamber (21.6 L/min for both chambers), a disturbed laminar flow was found, while at a flow rate of 560 mL/s (67.7 L/min in two chambers) the flow behaviour was mostly turbulent. Churchill et al. (2004) found that at the lowest flow rate of 0.1 L/min for water (equivalent to 1.5 L/min of inhaled air), either turbulent or 'transitional' flow was found in four cadaver replicate models. However, their working definition of a turbulent flow was based on visual inspection of whether eddies, cross-currents or mixing of dye were present.

Li et al. (2017) compared turbulence models against the experimental work of Hahn et al. (1993) replicating the geometry and conditions. The results confirmed that a laminar flow model was most suitable for 180 mL/s flow rate through a single nasal chamber (21.6 L/min for both chambers), and turbulent models were better suited for flow rates of 560 mL/s and greater. The study's single nasal chamber geometry omits the choana where flow streams from the left and right nasal chambers converge, and mix as two impinging jets. The nasopharynx was also omitted, where secondary flows, Dean vortices, and flow separation are found.

In previous work, a laminar flow assumption (Zhao et al., 2004; Subramaniam et al., 1998; Shang et al., 2015; Garcia et al., 2007; Elad et al., 2008; Ge et al., 2012; Goodarzi-Ardakani et al., 2016) was used for flow rates of 15 L/min or less. For higher flow rates (> 20 L/min), a turbulent flow field was assumed with varied selections of turbulent models. Early studies applied RANS (Reynolds Averaged Navier-Stokes) models including k-ε (Inthavong et al., 2006; Lindemann et al., 2005), k-ω models (Hörschler et al., 2006; Wen et al., 2008) and v^2-f (Inthavong et al., 2011). Kleinstreuer and Zhang (2003) demonstrated that to capture a laminar-transitional turbulent flow, a low-Reynolds-number (LRN) k-ω model was suitable. This model captures the transitional flow phenomena in the human airways and has since been adopted by other researchers (Zhu et al., 2013; Inthavong et al., 2014; Zhao and Jiang, 2014; Kim et al., 2012). At present, this model is accepted as one of the more suitable forms of RANS turbulence models, along with its variations (e.g. LRN k-ε and other transition models).

The Large Eddy Simulations (LES) (Calmet et al., 2016; Lee et al., 2010) and Direct Numerical Simulations (DNS) (Li et al., 2017) require significant computational resources and remain out of reach for large parametric studies or rapid clinical and engineering investigations. Moreover, these simulations require special care to define a high-quality mesh with high-order discretization schemes to minimise numerical diffusion, very small time-steps, and correct definitions of turbulence at the boundaries.

3.2. Steady versus unsteady flows

Breathing is a cyclic, oscillatory process. However, inhalation studies have predominantly simulated steady flow scenarios due to computational simplicity. A steady flow solution is representative of the mean flow field, smearing out any fluctuating or oscillating behaviour found in real cases. The significance of the fluctuations from the breathing cycle on the flow field can be estimated by examining the Womersley number, *Wo* or similarly the Strouhal number, *St*, defined as

$$Wo = \frac{D}{2}\left(\frac{\omega}{\nu}\right)^{0.5} \qquad St = \frac{\omega D}{u_{ave}}$$

where $\omega = 2\pi f = 1.57\ \mathrm{s}^{-1}$ is the nominal breathing frequency corresponding to approximately 15 breaths per minute (f); D is the characteristic length scale and can be defined by the average hydraulic diameter of 30 cross sections taken throughout the nasal cavity (Wen et al., 2008); u_{ave} is the average velocity through the nasal passage, which for a flow rate of 15 L/min is approximately 0.9 m/s. Wen et al. (2008) report Wo = 1.68 and $St = 0.01$, while Doorly et al. (2008) report $Wo = 3.0$ and $t = 0.25$ in their respective studies. The low Strouhal number, $St < 1$ along with the findings that oscillatory effects are not present until $Wo > 4$. (Isabey and Chang, 1981), suggest that the flow could be considered quasi-steady at low flow rates. This can be further emphasized from the study of Shi et al. (2006), who evaluated the influence of a waveform profile and showed only minor differences in the velocity contours between the accelerating and decelerating periods.

Unsteady flow modelling has been performed by Se et al. (2009) using a low-Reynolds Shear Stress Transport (SST) model, Kumar et al. (2016, 2017) used a laminar model, while Lee et al. (2010), Bahmanzadeh et al. (2015), Kumar et al. (2016), Calmet et al. (2016), and Bates et al. (2017) used an LES model. The justification

for laminar and low-Reynolds SST model comes from the predominantly lower flow rates during the respiration cycle. The exact breathing profiles are unique to an individual; in turn, Se et al. (2009), Lee et al. (2010), Calmet et al. (2016) applied profiles based on measured data while Kumar et al. (2016), Naseri et al. (2017), Bahmanzadeh et al. (2015) used a symmetrical sine wave form with a period of four seconds. If the simulations start from a zero (quiescent) state, two or three cycles are typically required to remove the start-up effects (hysteresis) to establish the transient solution.

3.3. Thermal models

An early study of the air conditioning capability of the nasal cavity was by Lindemann et al. (2004) accounting for temperature only. Lienar et al. (2003) also measured local nasal mucosal wall temperatures after exposure to air at different climatic conditions, which ranged between 32.3 °C and 34.7 °C for normal air and 30.6 °C and 33.7 °C for cold dry air conditions, respectively. These values were used as a baseline to define a uniform surface temperature of 32.6 °C (Garcia et al., 2007) and 32.1 °C (Inthavong et al., 2007). Burgos et al. (2014) found a linear relationship between the ambient temperature and the air average temperature reached along different cross sections in the nasal cavities.Other studies have included species transport equations for humidity as a concentration fraction (Naftali et al., 2005; Inthavong et al., 2007; Garcia et al., 2007). Kumahata et al. (2010) and Hanida et al. (2013) improved the modelling by using a wall boundary model that accounted for the latent heat in the heat exchange process, as well as moisture exchange. The results showed latent heat was most significant in the case of cold-dry inhaled air, and less significant for hot-humid inhaled air.

4. Nasal flow characteristics

The diverse nasal cavity morphology is influenced by demographic variations among subjects, which include age, sex, weight, and ethnicity (Zhu et al., 2011). It is also much more dynamic than computational models have been able to capture to date. For example, the airway continuously changes in shape and size from infants to adults, and then again in the elderly (Lindemann et al., 2008). In the shorter term, the geometry is subject to nasal cycling where partial congestion and decongestion alternate between the left/right nasal chambers. The nasal cycle is reported to occur on average every 4 h (Gyehwan et al., 2015), although its range was

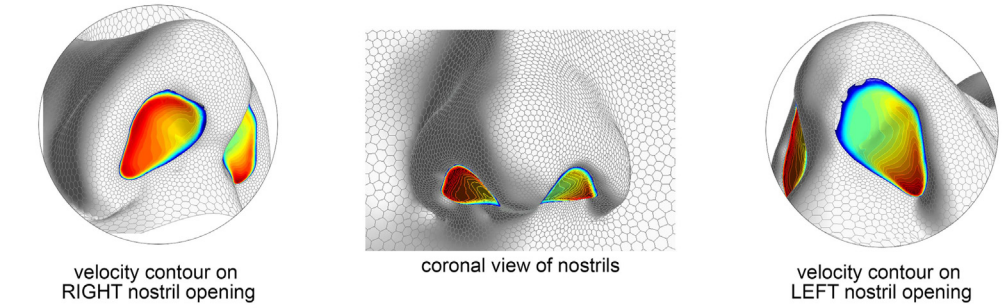

(a) Velocity contours at an irregular nostril opening surface.

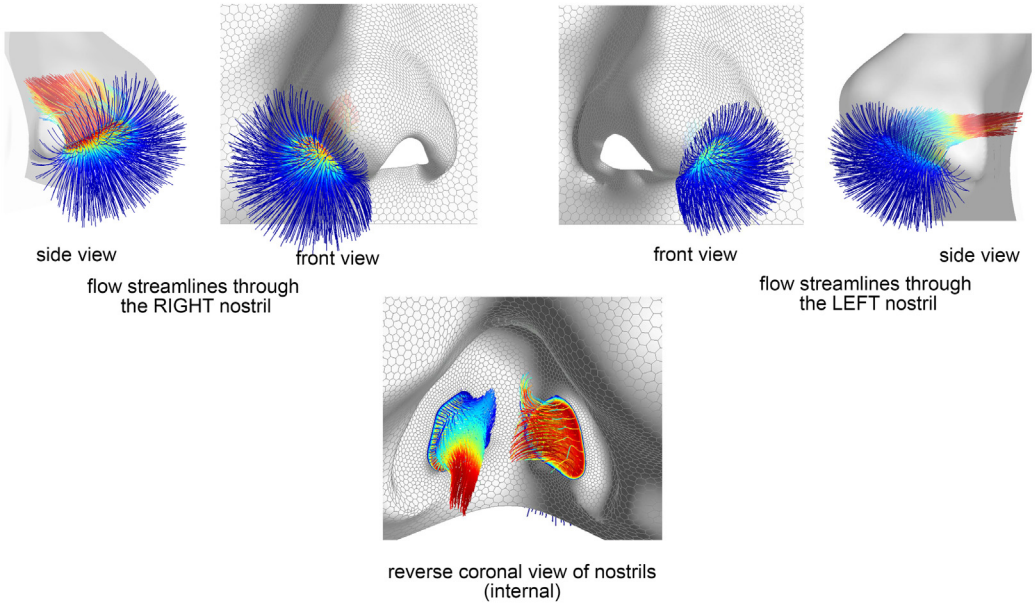

(b) Flow streamlines entering the two nostrils.

Fig. 7. Velocity contours and flow streamlines passing through the nostrils. The flow rate used was 10 L/min and the colour scheme uses blue = low velocity and red = high velocity. (For interpretation of the references to colour in this figure legend, the reader is referred to the web version of this article.)

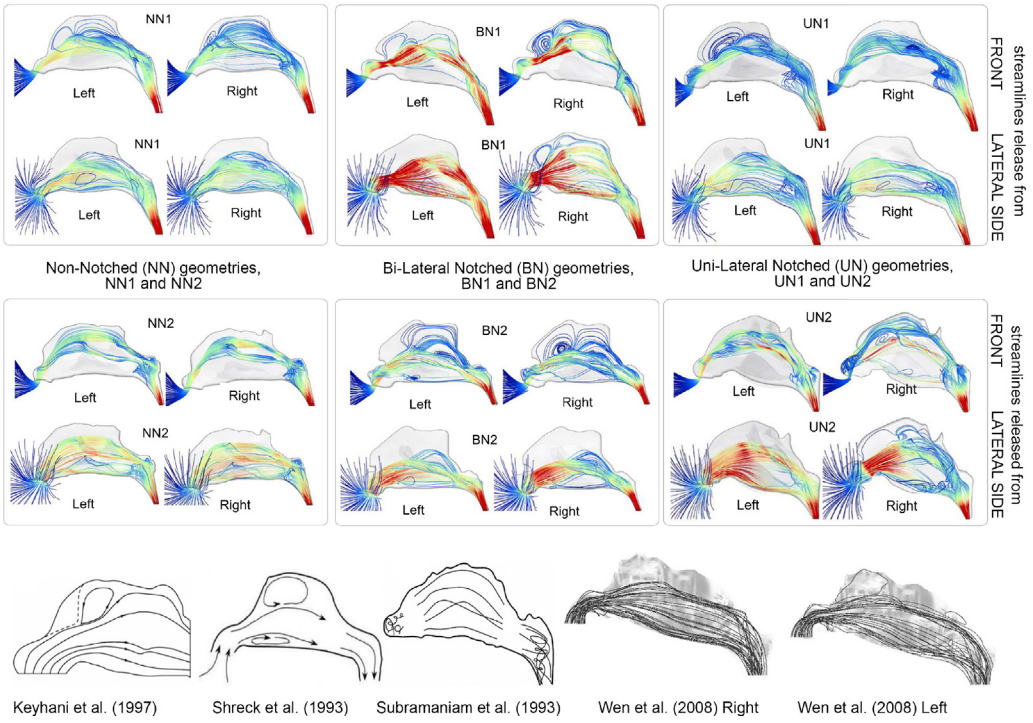

Fig. 8. Flow streamlines in ten nasal airway geometries extracted from Inthavong et al. (2017) and Wen et al. (2008). Geometries characterized by the presence of a notch in the anterior geometry. NN = 'no-notch', UN = 'Unilateral Notch'; BN = 'Bilateral Notch'. The suffixes 1 and 2 represent two different subjects within each category.

found between 25 min to 8 h with peak interval between 1.5–4 h during an awake state (Kahana-Zweig et al., 2016). It's also influenced by many factors including body posture (Eccles, 2000), sleep/awake state (Kahana-Zweig et al., 2016), and age (Mirza et al., 1997). Therefore, when scanned images of a patient are acquired, it is both patient specific and time dependent.

Geometry variations during breathing may include nasal valve collapse in the flexible cartilaginous walls of the external nose (Wittkopf et al., 2008), caused by sufficient pressure difference to trigger a venturi effect and, nasal valve enlargement through the actions of the nasal dilator muscles (Wustrow and Kastenbauer, 1995). Within the internal nasal cavity, the mucosal lining has the capacity to expand and contract. In particular, the inferior turbinate mucosa, along with the mucosa of the septal swell body (Mamikoglu et al., 2002), contains vascular erectile tissue that has the greatest capacity for fluctuation in size.

4.1. Entry into the nasal cavity

The nostrils are entry portals connecting the external environment with the internal nasal anatomy. The nostril inlet is typically non-planar, and its velocity distribution is also non-uniform. Fig. 7 presents a non-uniform velocity distribution on fitted surfaces (using a NURBS surfacing technique) of the nostril inlets. For the case shown, there is a clear bias to one corner in the left nostril, while for the right nostril, the contour is more evenly distributed. The flow streamlines show that the surrounding air converges into the nostril and rises upwards with an accelerated flow.

Results from Doorly et al. (2008) and Shang et al. (2015) have highlighted the need to include the external facial features and nostril as it helps reproduce the natural flow behaviour and inlet conditions. Xi et al. (2016) demonstrated the influence of nostril orientation on heat exchange and particle deposition using a range of angles from horizontally aligned to its more natural vertical orientation, recommending that the actual nostril angle should be preserved to predict more accurately respiratory functions.

4.2. Anterior nasal flow

After entering the nostrils, the vestibule area increases abruptly which produces flow separation and this can result in the formation of vortices (Zhao and Jiang, 2014). Fig. 8 shows a comparison of flow pathlines where the geometry BN2, and results from Subramaniam et al. (1998) exhibited vortices, but was absent in other models. The flow rapidly changes direction shifting to horizontal or at least angled towards the horizontal direction. As it enters the nasal valve region, which is the smallest cross sectional area, the flow accelerates. Studies (Doorly et al., 2008; Taylor et al., 2006; Zhao and Jiang, 2014) reported that a significant amount of pressure drop occurs in the nasal valve region and that the size and orientation of the nasal valve influences the downstream flow Doorly et al. (2008).

Ramprasad and Frank-Ito (2016) identified three distinct variations in the human nasal vestibule airspace among sixteen subjects with normal radiographic sinonasal images. Within each respective unilateral nasal cavity, the vestibule was classified as Notched, Standard, or Elongated phenotype based on nasal vestibule morphology, respectively. They found significant differences in flow resistance in localized regions of the different nasal vestibule phenotypes, but global comparisons from nostril to choana showed that average resistance was not significantly different. Similarly, for local differences in heat and mass transfer (Ma et al., 2018; Inthavong et al., 2018), and nanoparticle deposition in the upper passage and olfactory regions (Dong et al., 2018a), globally, both effects were less sensitive to the nasal vestibule phenotype.

Variations of the nose also include the outer nose geometry where its shape is characterised by the ratio of the width to the height of the external nose, called the nasal index, which was linked to ethnicity in Zhu et al. (2011). Zhao et al. (2004) and Li et al. (2018) found a significant correlation between nasal index and notch index where a narrower and taller external nose was more likely to have a pronounced notch, which may in turn lead to flow separation and formation of the vortex. Patki and Frank-Ito (2016) showed that

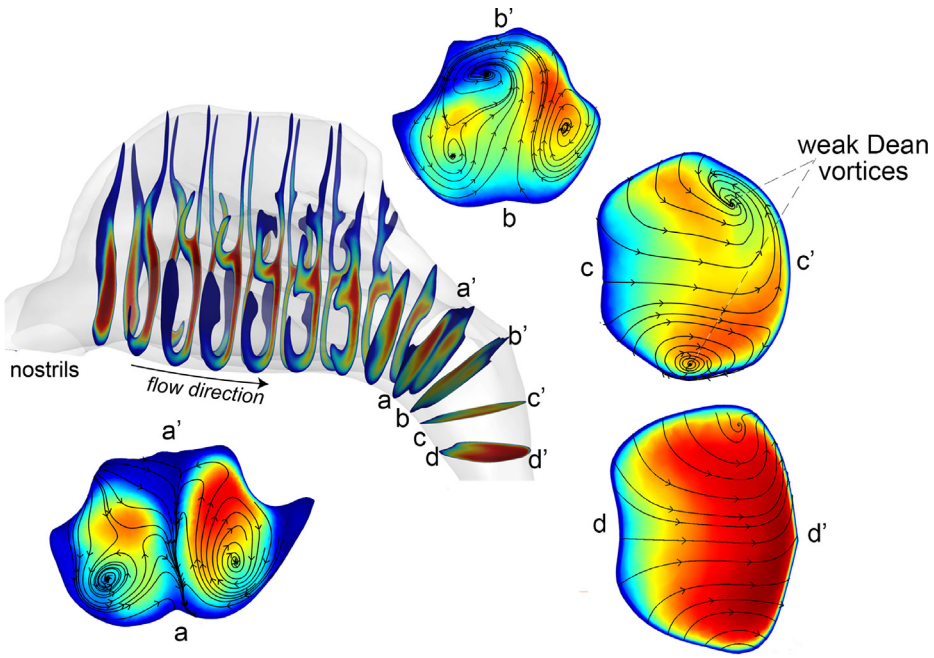

Fig. 9. Examples of velocity contours in the posterior nasal cavity. Flow direction is from left to right.

nasal index and nasal resistance were weakly correlated, and that a snasal index <80 had stronger correlations with wall shear stress and heat flux compared with a nasal index >80.

4.3. Flow in the main nasal passages

As air passes through the nasal valve, it enters the main nasal passage where the geometry diverges and expands. In many studies, this created a recirculating region (Fig. 8) or vortex in the upper anterior end of the nasal cavity (Wen et al., 2008; Doorly et al., 2008; Taylor et al., 2006; Zhao and Jiang, 2014). Lateral passages are formed by the turbinate bone protrusions where the flow is distributed between the inferior, middle and the superior meatus. Elad et al. (1993) found the airflow more streamlined due to the presence of turbinates since the flow was constrained in the narrowed passages, but some flow instabilities were found in dye visualization experiments in Doorly et al. (2008). Generally, airflow through the superior meatus is low while a more significant fraction passes through either the middle or the inferior meatus (Elad et al., 1993; Doorly et al., 2008; Zhu et al., 2011; Zhao and Jiang, 2014). The air also flows along the floor of the nasal cavity. These flow characteristics were subject to change depending on ethnicity where Zhu et al. (2011) found the middle passage of the nasal airway experienced more airflow in a Caucasian patient model whereas more flow passed through the inferior part for an Indian patient model. While the cross-sectional area increased after the nasal valve constriction, airflow velocities were similar or even higher compared to the anterior regions because of the narrowed passages.

4.4. Posterior nasal flow

The posterior nasal region consists of the choana where the two chambers merge and form a single conduit, and then turns 90° into the nasopharynx. Fig. 9 (slice a-a') shows that as the chamber merges, the flow streams remain separated with low velocities in the center. The merged air flow streams mix (slice b-b') with the flow shifting towards the posterior wall. Slice c-c' shows the development of weak secondary flows which produce the characteristic Dean vortices that are found in tubular bends geometries. Flow through the nasopharynx can therefore be characterised similar to a 90° bend with the key geometry feature being the bend curvature, and ellipsoidal diameter.

An important consequence of the nasopharynx bend is that it captures larger foreign particles at the posterior nasopharynx wall through inertial impaction. The geometry is also critical in determining the nature of airflow during expiration, when it acts as the upstream inlet condition to the nasal passage (Doorly et al., 2008). This can be important in drug delivery applications, which focus on delivering inhalation aerosols to targeted locations in the nose during expiration (Calmet et al., 2016).

5. Nasal cavity: physiology and function

The nasal airway geometry has evolved into a highly optimised structure that is efficient in many functions. The following section briefly summarises the functions of filtration, olfaction and air conditioning.

5.1. Filtration function

While, the major defense mechanism for trapping large particulates are the nasal vibrissae (hairs in the nostrils), the nasal vestibule bend into the main nasal passage also plays a role in particle capture. Large particles deposit onto the walls by inertial impaction when flow streamlines curve around bends too rapidly. This suggests that sharper nasal vestibule bends will contribute greater filtration capability Xi et al. (2016). The second bend at the nasopharynx acts as a second filter. Fig. 10 shows particle trajectories of 2.5, 10, and 20 μm and their deposition in a human nasal cavity as presented in Shang et al. (2015), where local concentrations of deposition caused by impaction of high inertial particles are found at the entrance into the main nasal passage and the nasopharynx.

The inertial parameter is used to describe inertial impaction caused by airway geometry, flow rate and particle size as a general prediction of particle filtration (Garcia et al., 2009; Tian et al., 2007; Liu et al., 2007; Shi et al., 2007). Fig. 11 shows the inertial parameter

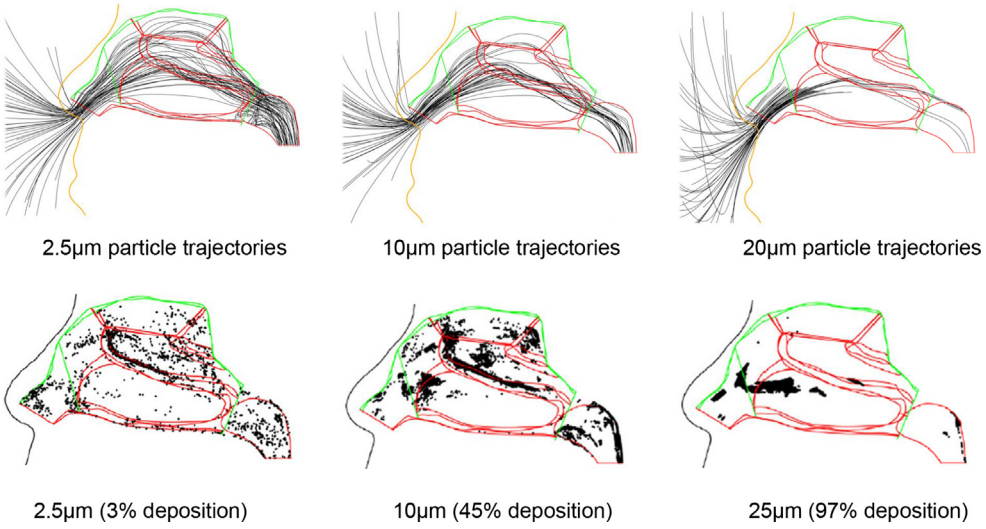

Fig. 10. Micron particle deposition by impaction (Shang et al., 2015).

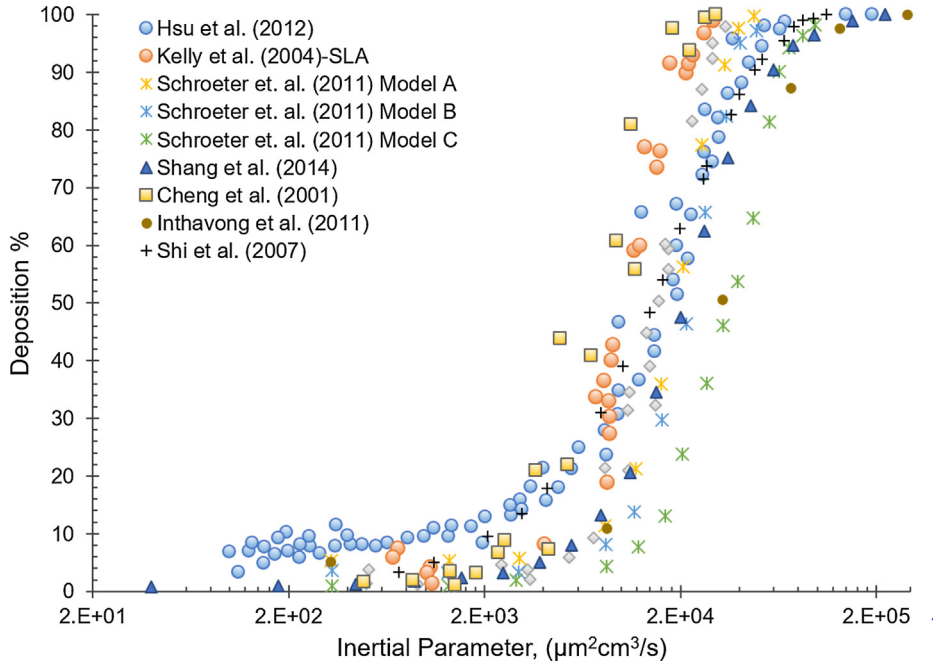

Fig. 11. Deposition efficiency curve for micron-sized particles as a function of the Inertial Parameter (IP) for various reported data.

results from different studies (Hsu and Chuang, 2012; Kelly et al., 2004; Schroeter et al., 2011; Shang et al., 2015; Cheng et al., 2001; Inthavong et al., 2011; Shi et al., 2007) which exhibits a sigmoidal profile. The inertial parameter (or impaction parameter) is a function of the particle size to the power 2, and the averaged inhalation flow rate (cm^3/s), suggesting a high sensitivity to particle size. Since the nasal cavity exhibits highly diverse anatomical variations, Garcia et al. (2009) proposed a modified Impaction Parameter as a function of the Stokes number to account for inter-individual variability in nasal filtration (see Fig. 12).

5.2. Olfaction function

Odorant perception is formed through interactions between airborne volatile chemical and olfactory receptors which are found on the olfactory epithelium, which is approximately a small 20 cm^2 patch of tissue buried in an aqueous mucus layer. Block (2015) stated that the olfactory region is found on the roof of the nasal cavity behind each nostril, while Leopold et al. (2000) found that the olfactory epithelium appeared to be distributed more anteriorly than the usual boundaries of the olfactory cleft depicted in textbooks. As inhaled odorant comes into contact with the mucus layer, it dissolves and passes through the mucus layer, and is detected by receptors that send electrical signals to the brain to provide the perception of smell.

Slow flows that move past the olfactory epithelium (see Fig. 8) increase residence times for gas uptake, since gas departure from the airflow must occur by a diffusion process. Zhao et al. (2004) and Wang et al. (2012) both state that lower flow rates allow more time for more odorant to be absorbed by the nasal/olfactory mucosa. Zhao et al. (2004) showed that small changes in the anatomy of nasal cavity at specific locations (e.g. nasal valve, turbinates)

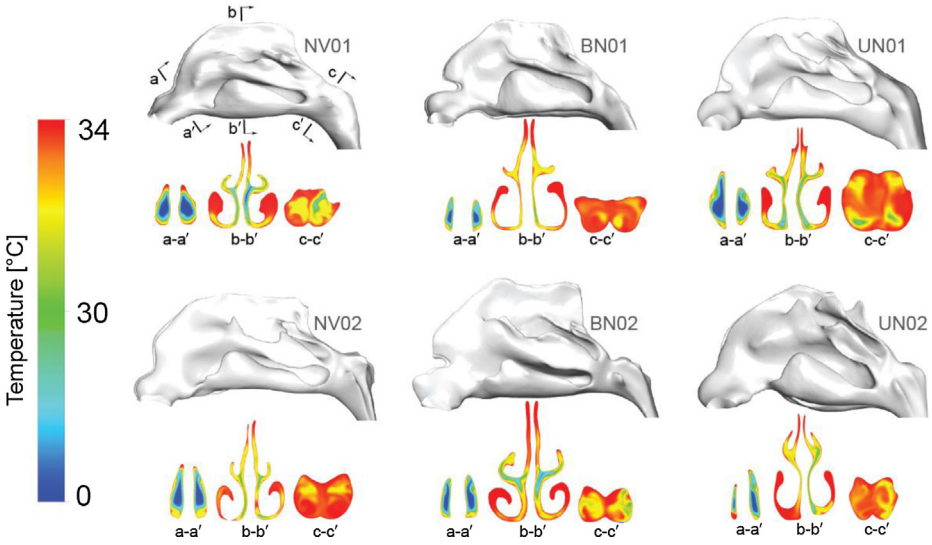

Fig. 12. Heat transfer in three nasal cavity models reported in Ma et al. (2018).

can induce large changes in the airflow affecting the odorant uptake on the olfactory mucosa. This has also been underlined in cases of moderate and severe nasal blockade (Lee et al., 2009) or as a consequence of middle turbinectomy (Alam et al., 2018), where higher velocities found in the olfactory groove led to negligible particle residence times, thus reduced odorant uptake. Nishijima et al. (2018) showed the olfactory airflow and olfaction were differentially affected by nasal polyp location. There has also been recent interest in the deposition of gases and particles targeting the olfactory region using computational studies focussing on toxicology (Tian et al., 2016) and drug delivery (Dong et al., 2018b), including magnetophoretic-guided drug particles (Xi et al., 2016). In both contrasting cases the deposition of gases and particles can lead to particle translocation into the brain.

5.3. Air conditioning function

The principles of heat (or mass) transfer take place in the presence of a temperature (or concentration) gradient. In the nasal cavity, this occurs through interaction between the inhaled air and the mucosal surface which is at a temperature of approximately 36 °C and at fully saturated state. Both surface temperature and moisture are regulated by a network of thin-walled blood vessels that lie underneath the nasal epithelium. The heat transfer rate is governed by $\dot{Q} = UA\Delta T$ where U is the overall heat transfer coefficient, ΔT is the temperature difference between the inhaled air and the surface temperature, and A is the surface area. The latter parameter explains the influence of the turbinates that protrude into the main passage which increases the mucosal surface area, enhancing the heating and conditioning of the inspired air.

CFD simulations of the air conditioning capability under different cases have been performed focussing on: air conditioning capacity (Naftali et al., 2005), septal perforation (Pless et al., 2004), atrophic rhinitus (Garcia et al., 2007), inferior turbinectomy (Lindemann et al., 2005; Chen et al., 2010), and inhalation of cold dry air (Inthavong et al., 2007). The results showed that the internal protrusions of the turbinates were vital to increase the heating and conditioning surface area in distributing the flow through different passages (i.e. meatii). A unanimous finding among the studies is the remarkable air conditioning capability of the nasal cavity

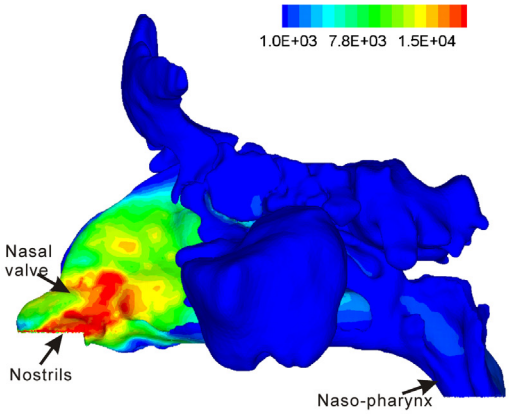

(a) Heat transfer flux contours.

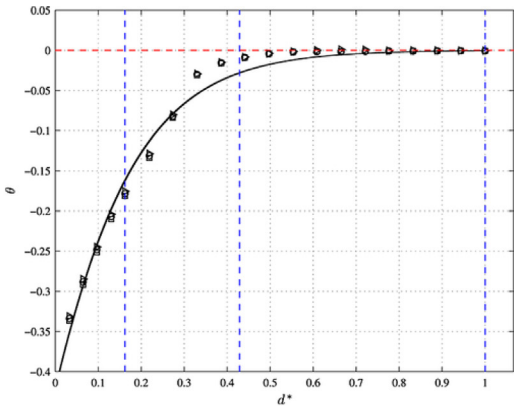

(b) Normalised temperature profile fitted for inhalation of cold, normal, and hot air.

Fig. 13. (a) Heat transfer flux contour obtained from Zhao et al. (2011), and (b) Normalised temperature profile for any inhalation condition from Burgos et al. (2014).

where the highest heat transfer rate takes place in the anterior regions of the nasal cavity (Fig. 13a), and in the inferior turbinate region.

Burgos et al. (2014) reported that air-conditioning along the depth of the nasal cavity takes place asymptotically. This is due to the diminishing temperature difference between the inhaled air and the mucus surface temperature through the nasal cavity, which is the driving contributor for heat transfer. They proposed a hyperbolic function (Fig. 13b) to characterize the temperature variation through the human nasal cavity, for both laminar and turbulent flows which could be used as a benchmark against a large population study.

6. Future research directions

6.1. Multiphysics applications

Complex models incorporating multiphysics are now within reach with advanced physics models and computational resources being made available. Transient flow modelling coupled with fluid-structure-interactions or at least moving (dynamic) mesh motion can provide dynamic modelling of physiological functions that are transient in nature. Application of elastic surfaces will be important for understanding the influence, and effective treatment of nasal valve collapse and collapse of the alae nasi.

Particle interaction with the mucus layer may also provide further analysis of drug delivery efficacy based on deposition rate. The nose's mucociliary function serves as a defense mechanism that provides a pathway for eventual dissolution into the mucus sublayers. Kirch et al. (2011) provided an early study on the effect of mucociliary clearance on nanoparticle deposition, while Rygg and Longest (2016) and later Shang et al. (in press) provided new methods for modelling the mucus motion and its influence on clearance mechanisms. An alternative technique is the Physiologically Based PharmacoKinetic (PBPK) model for predicting the absorption dosimetry analysis. Studies have incorporated PBPK with CFD (Yoo and Ito, 2018; Kimbell and Subramaniam, 2001; Schroeter et al., 2008) in toxicology studies where dosimetry flux can be determined through particle deposition rates onto the boundary walls.

6.2. Multiphase flows

Many fluid-particle studies (Naseri et al., 2017; Dong et al., 2019; Phuong et al., 2018; Inthavong, 2019) use one-way coupled Lagrangian models, but in nasal spray drug delivery, the region where spray atomization takes place, the particle/droplets are densely packed which influences the surrounding flow field. Future models will make use of different techniques e.g. dense-discrete-particle-modelling, two-way coupling, Eulerian-Eulerian multiphase, or even Volume-of-Fluid, to evaluate the fluid-particle and particle-particle interactions. A particle subject to shear will deform,and with sufficient deformation, will lead to particle breakup which needs to be quantified in spray models.

Studies have demonstrated the applicability of Volume-Of-Fluid modelling to investigate the liquid interface of nasal irrigation. This involves liquid flow entering the nasal cavity by a jet stream. Zhao et al. (2016) demonstrated its use to visualise sinus irrigations before and after surgery to evaluating irrigant penetration of individual sinus cavities. As an example, Fig. 14 shows our preliminary results using the Volume-Of-Fluid model to predict the sinus penetration of a liquid jet. The Volume-of-Fluid model can also track the interface in spray atomizers (Laurila et al., 2018; Belhadef et al., 2012). The model is limited for tracking individual particles since atomized particles are typically micron-sized and require mesh elements similar in size. A coupled Volume-of-Fluid and Discrete-Particle-Model (Liu and Luo, 2018) can be used to investigate in detail the particle behaviour for drug delivery in the nasal cavity.

6.3. CFD-assisted surgical planning

Diagnosis of disordered nasal airway for surgical planning may be assisted by objective tests, such as rhinomanometry which provide limited insight into the specific cause or site of obstruction. As a result, they provide little guidance to the appropriate choice of surgical interventions and most surgeons rely on clinical experience to determine the appropriate surgical interventions to consider.

Early attempts to model commonly-performed surgical procedures have been undertaken, including the effects of nasal airway surgery such as turbinate reduction surgery (Chen et al., 2010; Hariri et al., 2015; Lee et al., 2018) and septoplasty (Burgos et al., 2018; Frank-Ito et al., 2019) to improve nasal airflow and sinus

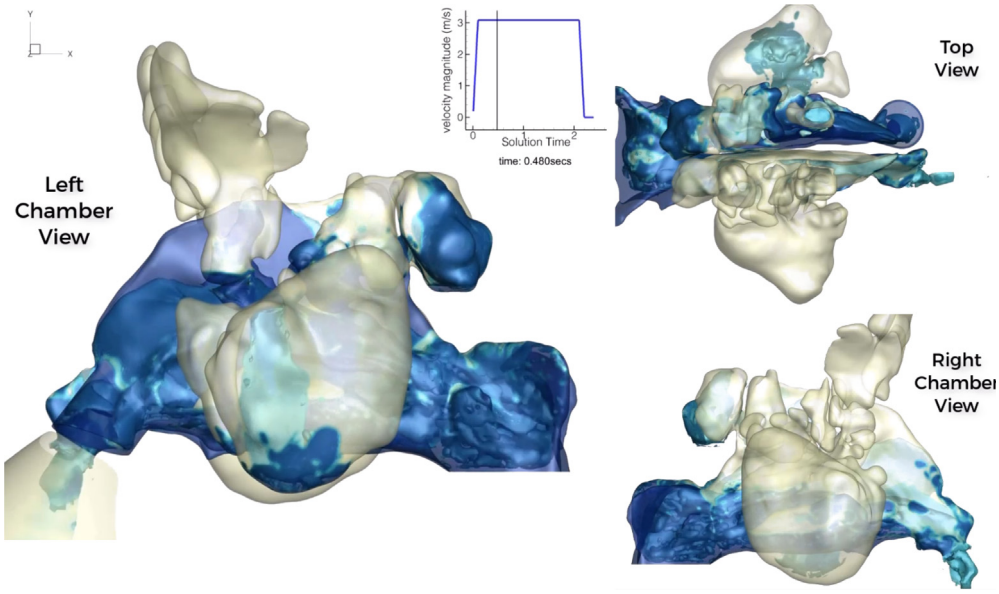

Fig. 14. Liquid jet penetration through a sino-nasal cavity model using the Volume-of-Fluid multiphase model.

surgery (Zhao et al., 2006) to improve sinus ventilation in chronic rhinosinusitis. However, in these instances, researchers have broadly only assessed the results of "virtual surgery" on CFD models. Post-operative changes have been modelled in cadaveric specimens in patients with unilateral sinus surgery (Chen et al., 2011), in single case reports of NAO surgery (Rhee et al., 2012; Zhu et al., 2014) and in small-scale series of patients undergoing NAO surgery (Sullivan et al., 2014).

One of the challenges of assessing the results of virtual surgery is in defining normal nasal airflow in healthy subjects (Zhao and Jiang, 2014) and the ideal or "gold standard" outcome. Ideally, virtual surgery should be performed on pre-operative CFD models of actual patients, then compared with post-operative CFD models of the same patients, along with clinical measures of nasal airflow, for a prospective cohort of patients. Other limitations of virtual surgery methods have been discussed: Quadrio et al. (2014) discussed procedural and modeling challenges that still prevent CFD, while (Pawar et al., 2010) emphasised that the integration of patient-reported outcome measures with objective data would certainly bring a new dimension to the analysis of nasal form and function in aesthetic and functional nasal surgery. The need for software to effectively translate virtual surgery steps into computational models has been discussed (Frank-Ito et al., 2014) and early attempts at such software have been recently described (Burgos et al., 2018; Cercos-Pita et al., 2018).

Early studies of virtual surgery include the effects of septal surgery and, turbinate surgery (Chen et al., 2010). Rhee et al. (2011) applied virtual surgery on 3D nasal airway models to assess functional outcomes of nasal surgery through CFD, and showed its potential as a predictive tool to enable surgeons to perform personalized nasal surgery. Burgos et al. (2018) developed an integrated computational platform to perform virtual surgery to choose the best improvement in nasal flow. Vanhille et al. (2018) showed that using a virtual surgery planning tool had a potential role for patient counselling, and identifying which anatomical structures should be targeted for surgical correction. These studies suggest that future surgical planning may eventually adopt some form of CFD-assistance.

6.4. Applications of big data in nasal airway modelling

A drawback of CFD modelling is the high need for computational storage and lengthy computational time, particularly for transient flows. The prospect of using Artificial Neural Network (ANN) may provide rapid results as an alternative to CFD models. Its accuracy is reliant on training samples and the algorithm used for machine learning to describe the fluid dynamics behaviour. Its application includes automated airway segmentation from CT/MRI scans, and virtual surgery to determine an optimal surgical strategy. Eventually, machine learning could suggest the best surgical technique simply from scanned CT/MR data.

Optimised and personalised health care will rely on massive data (e.g. *Big Data* concept) leading to the next revolution in health care in the so-called Digital Twin. This term refers to the digital representation of a physical product such as the human anatomy. With the development of the *Internet of Things* (IoT), digital twins are becoming a potential across many industries, including healthcare, and it is expected that with machine learning, this will become a reality. However, its success is anticipated to rely on large data sets and well established results to ensure that the computational analysis will provide reliable results.

7. Conclusion

The growing research interest in computational fluid modelling of the nasal airway coincides with the 25th year landmark since the first few computational studies were published. As this multi-disciplinary field emerged, computational modelling techniques also advanced. This review showed that there were new methods that were pertinent to accuracy - such as influence of segmentation, mesh independence evaluations, and inclusion of the external face and nostril openings. Flow regime (i.e. laminar vs. turbulent) and the applicability of steady or unsteady flow representations remain controversial, such that best practices should be applied for either cases used.

The future of computational modelling of the airway will be driven by advances in multiphysics. It will also be swept along with the current explosion in Artificial Intelligence which have already impacted the CFD field. The growth in this discipline and computational advancements will bring new opportunities and significant breakthroughs in this exciting field.

Acknowledgement

This work was supported by the Garnett Passe, Rodney Williams Memorial Foundation Conjoint Grant (2019-CG-Inthavong-Singh), and the European Research Council (ERC) under the European Union's Horizon 2020 research and innovation program (grant agreement No. 677772).

References

Adil, E., Huntley, C., Choudhary, A., Carr, M., 2012. Congenital nasal obstruction: clinical and radiologic review. Eur. J. Pediatr. 171 (4), 641–650. https://doi.org/10.1007/s00431-011-1591-6.

Alam, S., Li, C., Bradburn, K.H., Zhao, K., Lee, T.S., 2018. Impact of middle turbinectomy on airflow to the olfactory cleft: a computational fluid dynamics study. Am. J. Rhinol. Allergy 1945892418816841, pMID: 30543120. doi:https://doi.org/10.1177/1945892418816841.

Anderson, J., 1995. Computational Fluid Dynamics. McGraw-Hill Education <https://books.google.com.au/books?id=dJceAQAAIAAJ>.

Bahmanzadeh, H., Abouali, O., Faramarzi, M., Ahmadi, G., 2015. Numerical simulation of airflow and micro-particle deposition in human nasal airway pre- and post-virtual sphenoidotomy surgery. Comput. Biol. Med. 61, 8–18 <http://www.sciencedirect.com/science/article/pii/S0010482515000931>.

Bass, K., Worth Longest, P., 2018. Recommendations for simulating microparticle deposition at conditions similar to the upper airways with two-equation turbulence models. J. Aerosol Sci. 119, 31–50.

Bates, A.J., Schuh, A., Amine-Eddine, G., McConnell, K., Loew, W., Fleck, R.J., Woods, J. C., Dumoulin, C.L., Amin, R.S., 2017. Assessing the relationship between movement and airflow in the upper airway using computational fluid dynamics with motion determined from magnetic resonance imaging. Clin. Biomech.

Belhadef, A., Vallet, A., Amielh, M., Anselmet, F., 2012. Pressure-swirl atomization: modeling and experimental approaches. Int. J. Multiph. Flow 39, 13–20 <http://www.sciencedirect.com/science/article/pii/S0301932211002096>.

Block, E., 2015. What's that smell? A controversial theory of olfaction deemed implausible. Conversation.

Bui, N.L., Ong, S.H., Foong, K.W.C., 2015. Automatic segmentation of the nasal cavity and paranasal sinuses from cone-beam ct images. Int. J. Comput. Assist. Radiol. Surg. 10 (8), 1269–1277.

Burgos, M., Sanmiguel-Rojas, E., Singh, N., Esteban-Ortega, F., 2018. Digbody: A new 3d modeling tool for nasal virtual surgery. Comput. Biol. Med. 98, 118–125 <http://www.sciencedirect.com/science/article/pii/S001048251830129X>.

Burgos, M., Sanmiguel-Rojas, E., Martin-Alcantara, A., Hidalgo-Martinez, M., 2014. Effects of the ambient temperature on the airflow across a caucasian nasal cavity. Int. J. Numer. Meth. Biomed. Eng. 30, 430–445.

Burgos, M.A., Sanmiguel-Rojas, E., Pino, C.D., Sevilla-García, M.A., Esteban-Ortega, F., 2017. New cfd tools to evaluate nasal airflow. Eur. Arch. Otorhinolaryngol. 274, 3121–3128.

Cai, J., Chang, Z., Wang, Z., Paul Segars, W., Yin, F.F., 2011. Four-dimensional magnetic resonance imaging (4d-mri) using image-based respiratory surrogate: a feasibility study. Med. Phys. 38 (12), 6384–6394.

Calmet, H., Gambaruto, A.M., Bates, A.J., Vazquez, M., Houzeaux, G., Doorly, D.J., 2016. Large-scale cfd simulations of the transitional and turbulent regime for the large human airways during rapid inhalation. Comput. Biol. Med. 69, 166–180.

Cercos-Pita, J., Cal, I., Duque, D., de Moreta, G.S., 2018. Nasal-geom, a free upper respiratory tract 3d model reconstruction software. Comput. Phys. Commun. 223, 55–68.

Chen, X., Leong, S.C., Lee, H.P., Chong, V.F., Wang, D.Y., 2010. Aerodynamic effects of inferior turbinate surgery on nasal airflow – a computational fluid dynamics model. Rhinology 48 (4), 394–400.

Chen, X.B., Lee, H., Chong, V., Wang, D.E.Y., 2011. Aerodynamic characteristics inside the rhino-sinonasal cavity after functional endoscopic sinus surgery. Am. J. Rhinol. Allergy 25, 388–392.

Chen, X.B., Lee, H.P., Chong, V.F.H., Wang, D.Y., 2010. Numerical simulation of the effects of inferior turbinate surgery on nasal airway heating capacity. Am. J. Rhinol. Allergy 24 (5), e118–e122. https://doi.org/10.2500/ajra.2010.24.3511.

Cheng, Y., Holmes, T., Gao, J., Guilmette, R., Li, S., Surakitbanharn, Y., Rowlings, C., 2001. Characterization of nasal spray pumps and deposition pattern in a replica of the human nasal airway. J. Aerosol Med. 14 (2), 267–280. https://doi.org/10.1089/08942680152484199, pMID: 11681658.

Churchill, S., Shackelford, L.L., Georgi, N., Black, M., 2004. Morphological variation and airflow dynamics in the human nose. Am. J. Hum. Biol. 16, 625–638.

Corey, J.P., Gungor, A., Nelson, R., Fredberg, J., Lai, V., 1997. A comparison of the nasal cross-sectional areas and volumes obtained with acoustic rhinometry and magnetic resonance imaging. Otolaryngol.-Head Neck Surg. 117 (4), 349–354. https://doi.org/10.1016/S0194-5998(97)70125-6, pMID: 9339795.

Dong, J., Ma, J., Shang, Y., Inthavong, K., Qiu, D., J., T., Frank-Ito, D., 2018a. Detailed nanoparticle exposure analysis among human nasal cavities with distinct vestibule phenotypes. J. Aerosol Sci. 121, 54–65 <http://www.sciencedirect.com/science/article/pii/S0021850218300193>.

Dong, J., Shang, Y., Inthavong, K., Chan, H.-K., Tu, J., 2018b. Partitioning of dispersed nanoparticles in a realistic nasal passage for targeted drug delivery. Int. J. Pharm. 543 (1), 83–95 http://www.sciencedirect.com/science/article/pii/S0378517318301935.

Dong, J., Tian, L., Ahmadi, G., 2019. Numerical assessment of respiratory airway exposure risks to diesel exhaust particles. Exp. Comput. Multiphase Flow 1 (1), 51–59. https://doi.org/10.1007/s42757-019-0005-2.

Doorly, D.J., Taylor, D.J., Schroter, R.C., 2008. Mechanics of airflow in the human nasal airways. Respirat. Physiol. Neurobiol. 163 (1–3), 100–110.

Eccles, R., 2000. The nasal cycle in respiratory defence. Acta oto-rhino-laryngologica Belgica 54 (3), 281–286.

Elad, D., Liebenthal, R., Wenig, B.L., Einav, S., 1993. Analysis of air flow patterns in the human nose. Med. Biol. Eng. Comput. 31 (6), 585–592.

Elad, D., Wolf, M., Keck, T., 2008. Air-conditioning in the human nasal cavity. Respirat. Physiol. Neurobiol. 163 (1), 121–127. respiratory Biomechanics <http://www.sciencedirect.com/science/article/pii/S1569904808001262>.

Fletcher, C., 2013. Computational Techniques for Fluid Dynamics 1: Fundamental and General Techniques. Springer, Berlin Heidelberg <https://books.google.com.au/books?id=T2TyCAAAQBAJ>.

Frank-Ito, D.O., Kimbell, J.S., Borojeni, A.A.T., Garcia, G.J.M., Rhee, J.S., 2019. A hierarchical stepwise approach to evaluate nasal patency after virtual surgery for nasal airway obstruction. Clin. Biomech. 61, 172–180. https://doi.org/10.1016/j.clinbiomech.2018.12.014.

Frank-Ito, D.O., Kimbell, J.S., Laud, P., Garcia, G.J.M., Rhee, J.S., 2014. Predicting postsurgery nasal physiology with computational modeling:current challenges and limitations. Otolaryngol.-Head Neck Surg. 151 (5), 751–759 <https://journals.sagepub.com/doi/abs/10.1177/0194599814547497>.

Frank-Ito, D.O., Wofford, M., Schroeter, J.D., Kimbell, J.S., 2015. Influence of mesh density on airflow and particle deposition in sinonasal airway modeling. J. Aerosol. Med. Pulm. Drug. Deliv.

Garcia, G.J.M., Bailie, N., Martins, D.A., Kimbell, J.S., 2007. Atrophic rhinitis: a cfd study of air conditioning in the nasal cavity. J. Appl. Physiol. 103 (3), 1082–1092. https://doi.org/10.1152/japplphysiol.01118.2006, pMID: 17569762.

Garcia, G.J.M., Tewksbury, E.W., Wong, B.A., Kimbell, J.S., 2009. Interindividual variability in nasal filtration as a function of nasal cavity geometry. J. Aerosol Med. Pulmonary Drug Delivery 22 (2), 139–155.

Ge, Q., Inthavong, K., Tu, J.Y., 2012. Local deposition fractions of ultrafine particles in a human nasal-sinus cavity cfd model. Inhalation Toxicol. 24, 492–505.

Goodarzi-Ardakani, V., Taeibi-Rahni, M., Salimi, M., Ahmadi, G., 2016. Computational simulation of temperature and velocity distribution in human upper respiratory airway during inhalation of hot air. Respirat. Physiol. Neurobiol. 223, 49–58 <http://www.sciencedirect.com/science/article/pii/S1569904816300015>.

Gyehwan, J., Seung-Kyu, C., Yang, N., 2015. Numerical study of the effect of the nasal cycle on unilateral nasal resistance. Respirat. Physiol. Neurobiol. 219, 58–68 <http://www.sciencedirect.com/science/article/pii/S1569904815300355>.

Hahn, I., Scherer, P.W., Mozell, M.M., 1993. Velocity profiles measured for airflow through a large-scale model of the human nasal cavity. J. Appl. Physiol. 75 (5), 2273–2287. https://doi.org/10.1152/jappl.1993.75.5.2273, pMID: 8307887.

Hanida, S., Mori, F., Kumahata, K., Watanabe, M., Ishikawa, S., Matsuzawa, T., 2013. Influence of latent heat in the nasal cavity. J. Biomech. Sci. Eng. 8 (3), 209–224.

Hariri, B.M., Rhee, J.S., Garcia, G.J.M., 2015. Identifying patients who may benefit from inferior turbinate reduction using computer simulations. Laryngoscope 125 (12), 2635–2641.

Hörschler, I., Brücker, C., Schröder, W., Meinke, M., 2006. Investigation of the impact of the geometry on the nose flow. Eur. J. Mech. B. Fluids 25 (4), 471–490 <http://www.sciencedirect.com/science/article/pii/S0997754606000045>.

Hsu, D.-J., Chuang, M.-H., 2012. In-vivo measurements of micrometer-sized particle deposition in the nasal cavities of taiwanese adults. Aerosol Sci. Technol. 46 (6), 631–638. https://doi.org/10.1080/02786826.2011.652749.

Inthavong, K., Ge, Q.J., Li, X.D., Tu, J.Y., 2012. Detailed predictions of particle aspiration affected by respiratory inhalation and airflow. Atmospheric Environment 62, 107–117. https://doi.org/10.1016/j.atmosenv.2012.07.071.

Inthavong, K., 2019. A unifying correlation for laminar particle deposition in 90-degree pipe bends. Powder Technol. 345, 99–110 <http://www.sciencedirect.com/science/article/pii/S003259101831132X>.

Inthavong, K., Chetty, A., Shang, Y., Tu, J., 2018. Examining mesh independence for flow dynamics in the human nasal cavity. Comput. Biol. Med. 102, 40–50 <http://www.sciencedirect.com/science/article/pii/S0010482518302725>.

Inthavong, K., Ma, J., Shang, Y., Dong, J., Chetty, A.S., Tu, J., Frank-Ito, D., 2017. Geometry and airflow dynamics analysis in the nasal cavity during inhalation. Clin. Biomech.

Inthavong, K., Shang, Y.D., Tu, J.Y., 2014. Surface mapping for visualization of wall stresses during inhalation in a human nasal cavity. Respirat. Physiol. Neurobiol. 190 (54–61).

Inthavong, K., Tian, Z., Tu, J., 2007. Cfd simulations on the heating capability in a human nasal cavity. In: 16th Australasian Fluid Mechanics Conference (AFMC). School of Engineering, The University of Queensland, pp. 842–847.

Inthavong, K., Tian, Z., Tu, J., Yang, W., Xue, C., 2008. Optimising nasal spray parameters for efficient drug delivery using computational fluid dynamics. Comput. Biol. Med. 38 (6), 713–726 <http://www.sciencedirect.com/science/article/pii/S0010482508000528>.

Inthavong, K., Tian, Z.F., Li, H.F., Tu, J.Y., Yang, W., Xue, C.L., Li, C.G., 2006. A numerical study of spray particle deposition in a human nasal cavity. Aerosol Sci. Technol. 40 (11), 1034–1045. <Go to ISI>://WOS:000240835800008..

Inthavong, K., Tu, J., Heschl, C., 2011. Micron particle deposition in the nasal cavity using the v2–f model. Comput. Fluids 51 (1), 184–188 <http://www.sciencedirect.com/science/article/pii/S0045793011002568>.

Inthavong, K., Wen, J., Tian, Z., Tu, J., 2008. Numerical study of fibre deposition in a human nasal cavity. J. Aerosol Sci. 39 (3), 253–265.

Isabey, D., Chang, H., 1981. Steady and unsteady pressure-flow relationships in central airways. J. Appl. Physiol. 51, 1338–1348.

Kahana-Zweig, R., Geva-Sagiv, M., Weissbrod, A., Secundo, L., Soroker, N., Sobel, N., 2016. Measuring and characterizing the human nasal cycle. PLoS One 11 (10), e0162918.

Kase, Y., Hilberg, O., Pedersen, O., 1994. Posture and nasal patency: evaluation by acoustic rhinometry. Acta Otolaryngol. 114 (1), 70–74.

Kelly, J.T., Asgharian, B., Kimbell, J.S., Wong, B.A., 2004. Particle deposition in human nasal airway replicas manufactured by different methods. part i: Inertial regime particles. Aerosol Sci. Technol. 38 (11), 1063–1071. https://doi.org/10.1080/027868290883360.

Keyhani, K., Scherer, P.W., Mozell, M.M., 1995. Numerical simulation of airflow in the human nasal cavity. J. Biomech. Eng. 117 (4), 429–441.

Kim, J.W., Xi, J., Si, X.A., 2012. Dynamic growth and deposition of hygroscopic aerosols in the nasal airway of a 5-year-old child. Int. J. Numer. Methods Biomed. Eng. 29 (1), 17–39 <https://onlinelibrary.wiley.com/doi/abs/10.1002/cnm.2490>.

Kimbell, J., Subramaniam, R., 2001. Use of computational fluid dynamics models for dosimetry of inhaled gases in the nasal passages. Inhalation Toxicol. 13 (5), 325–334. https://doi.org/10.1080/08958370120442.

Kimura, S., Sakamoto, T., Sera, T., Yokota, H., Ono, K., Doorly, D.J., Schroter, R.C., Tanaka, G., 2019. Voxel-based modeling of airflow in the human nasal cavity. Comput. Methods Biomech. Biomed. Eng. 22 (3), 331–339. https://doi.org/10.1080/10255842.2018.1555584, pMID: 30773052.

King Se, C.M., Inthavong, K., Tu, J., 2010. Inhalability of micron particles through the nose and mouth. Inhalation Toxicol. 22 (4), 287–300.

Kirch, J., Guenther, M., Schaefer, U.F., Schneider, M., Lehr, C.-M., 2011. Computational fluid dynamics of nanoparticle disposition in the airways: mucus interactions and mucociliary clearance. Comput. Vis. Sci. 14 (7), 301–308. https://doi.org/10.1007/s00791-012-0184-x.

Kleinstreuer, C., Zhang, Z., 2003. Laminar-to-turbulent fluid-particle flows in a human airway model. Int. J. Multiphase Flow 29, 271.

Kumahata, K., Mori, F., Ishikawa, S., Matsuzawa, T., 2010. Nasal flow simulation using heat and humidity models. J. Biomech. Sci. Eng. 5 (5), 565–577.

Kumar, H., Jain, R., Douglas, R.G., Tawhai, M.H., 2016. Airflow in the human nasal passage and sinuses of chronic rhinosinusitis subjects. PLoS One 11, e0156379.

Kwong, Y., Mel, A.O., Wheeler, G., Troupis, J.M., 2015. Four-dimensional computed tomography (4dct): a review of the current status and applications. J. Med. Imaging Radiat. Oncol. 59 (5), 545–555.

Laurila, E., Roenby, J., Maakala, V., Peltonen, P., Kahila, H., Vuorinen, V., 2018. Analysis of viscous fluid flow in a pressure-swirl atomizer using large-eddy simulation. Int. J. Multiphase Flow <http://www.sciencedirect.com/science/article/pii/S0301932218303239>.

Lee, H., Poh, H., Chong, F., Wang De, Y., 2009. Changes of airflow pattern in inferior turbinate hypertrophy: a computational fluid dynamics model. Am. J. Rhinol. Allergy 23 (2), 153–158.

Lee, J.-H., Na, Y., Kim, S.-K., Chung, S.-K., 2010. Unsteady flow characteristics through a human nasal airway. Respirat. Physiol. Neurobiol. 172 (3), 136–146 <http://www.sciencedirect.com/science/article/pii/S1569904810001850>.

Lee, T.S., Goyal, P., Li, C., Zhao, K., 2018. Computational fluid dynamics to evaluate the effectiveness of inferior turbinate reduction techniques to improve nasal airflow. JAMA Facial Plastic Surg. 20 (4), 263.

Leopold, D.A., Hummel, T., Schwob, J.E., Hong, S.C., Knecht, M., Kobal, G., 2000. Anterior distribution of human olfactory epithelium. Laryngoscope 110 (3), 417–421.

Li, C., Jiang, J., Dong, H., Zhao, K., 2017. Computational modeling and validation of human nasal airflow under various breathing conditions. J. Biomech. 64, 59–68 <http://www.sciencedirect.com/science/article/pii/S0021929017304542>.

Li, C., Jiang, J., Kim, K., Otto, B.A., Farag, A.A., Cowart, B.J., Pribitkin, E.A., Dalton, P., Zhao, K., 2018. Nasal structural and aerodynamic features that may benefit normal olfactory sensitivity. Chem. Senses 43 (4), 229–237. https://doi.org/10.1093/chemse/bjy013.

Lienar, K., Leiacker, R., Lindemann, J., G., R., Keck, T., 2003. Nasal mucosal temperature after exposure to cold, dry air and hot, humid air. Acta Otolaryngol. 123, 851–856.

Lindemann, J., Brambs, H.-J., Keck, T., Wiesmiller, K., Rettinger, G., Pless, D., 2005. Numerical simulation of intranasal airflow after radical sinus surgery. Am. J. Otolaryngol. 26 (3), 175–180 <http://www.sciencedirect.com/science/article/pii/S0196070905000396>.

Lindemann, J., Keck, T., Wiesmiller, K., Rettinger, G., Brambs, H., Pless, D., 2005. Numerical simulation of intranasal air flow and temperature after resection of the turbinates. Rhinology 43, 24–28.

Lindemann, J., Keck, T., Wiesmiller, K., Sander, B., Brambs, H., Rettinger, G., Pless, P., 2004. A numerical simulation of intranasal air temperature during inspiration. Laryngoscope 114, 1037–1041.

Lindemann, J., Sannwald, D., Wiesmiller, K., 2008. Age-related changes in intranasal air conditioning in the elderly. Laryngoscope 118, 1472–1475.

Lintermann, A., Schröder, W., 2017. A hierarchical numerical journey through the nasal cavity: from nose-like models to real anatomies. Flow Turbul. Combust.

Liu, Q., Luo, Z.-H., 2018. Cfd-vof-dpm simulations of bubble rising and coalescence in low hold-up particle-liquid suspension systems. Powder Technol. 339, 459–469 <http://www.sciencedirect.com/science/article/pii/S0032591018306715>.

Liu, Y., Matida, E., Junjie, G., Johnson, M., 2007. Numerical simulation of aerosol deposition in a 3-d human nasal cavity using rans, rans/eim, and les. J. Aerosol Sci. 38 (7), 683–700.

Ma, J., Dong, J., Shang, Y., Inthavong, K., Tu, J., Frank-Ito, D.O., 2018. Air conditioning analysis among human nasal passages with anterior anatomical variations. Med. Eng. Phys. 57, 19–28 <http://www.sciencedirect.com/science/article/pii/S135045331830064X>.

Mamikoglu, B., Houser, S.M., Corey, J.P., 2002. An interpretation method for objective assessment of nasal congestion with acoustic rhinometry. Laryngoscope 112 (5), 926–929.

Mirza, N., Kroger, H., Doty, R.L., 1997. Influence of age on the 'nasal cycle'. Laryngoscope 107 (1), 62–66.

Miyawaki, S., Hoffman, E., Lin, C., 2016. Effect of static vs. dynamic imaging on particle transport in ct-based numerical models of human central airways. J. Aerosol Sci. 100, 129–139.

Naftali, S., Rosenfeld, M., Wolf, M., Elad, D., 2005. The air-conditioning capacity of the human nose. Ann. Biomed. Eng. 33 (4), 545–553. https://doi.org/10.1007/s10439-005-2513-4.

Naseri, A., Shaghaghian, S., Abouali, O., Ahmadi, G., 2017. Numerical investigation of transient transport and deposition of microparticles under unsteady inspiratory flow in human upper airways. Respirat. Physiol. Neurobiol. 244, 56–72 <http://www.sciencedirect.com/science/article/pii/S1569904817300447>.

Neelapu, B.C., Kharbanda, O.P., Sardana, V., Gupta, A., Vasamsetti, S., Balachandran, R., Rana, S.S., Sardana, H.K., 2017. A pilot study for segmentation of pharyngeal and sino-nasal airway subregions by automatic contour initialization. Int. J. Comput. Assist. Radiol. Surg. 12 (11), 1877–1893.

Negley, J.E., Krause, H., Pawar, S., Reeves-Hoché, M.K., 1999. Rinoflow nasal wash and sinus system as a mechanism to deliver medications to the paranasal sinuses: results of a radiolabeled pilot study. Ear Nose Throat J. 78 (8), 550–554. https://doi.org/10.1177/014556139907800808, pMID: 10485146.

Nishijima, H., Kondo, K., Yamamoto, T., Nomura, T., Kikuta, S., Shimizu, Y., Mizushima, Y., Yamasoba, T., 2018. Influence of the location of nasal polyps on olfactory airflow and olfaction. Int. Forum Allergy Rhinol. 8, 695–706.

Pal, N.R., Pal, S.K., 1993. A review on image segmentation techniques. Pattern Recognit. 26 (9), 1277–1294.

Patki, A., Frank-Ito, D.O., 2016. Characterizing human nasal airflow physiologic variables by nasal index. Respirat. Physiol. Neurobiol. 232, 66–74.

Pawar, S.S., Garcia, G.J.M., Kimbell, J.S., Rhee, J.S., 2010. Objective measures in aesthetic and functional nasal surgery: perspectives on nasal form and function. Facial Plast. Surg. 26 (04), 320–327.

Phuong, N.L., Khoa, N.D., Inthavong, K., Ito, K., 2018. Particle and inhalation exposure in human and monkey computational airway models. Inhalation Toxicol. 30 (11–12), 416–428. https://doi.org/10.1080/08958378.2018.1545810, pMID: 30618352.

Pless, D., Keck, T., Wiesmiller, K.M., Lamche, R., Aschoff, A.J., Lindemann, J., 2004. Numerical simulation of airflow patterns and air temperature distribution during inspiration in a nose model with septal perforation. Am. J. Rhinol. 18 (6), 357–362. https://doi.org/10.1177/194589240401800603.

Quadrio, M., Pipolo, C., Corti, S., Lenzi, R., Messina, F., Pesci, C., Felisati, G., 2014. Review of computational fluid dynamics in the assessment of nasal air flow and analysis of its limitations. Eur. Arch. Otorhinolaryngol. 271 (9), 2349–2354. https://doi.org/10.1007/s00405-013-2742-3.

Ramprasad, V.H., Frank-Ito, D.O., 2016. A computational analysis of nasal vestibule morphologic variabilities on nasal function. J. Biomech. 49 (3), 450–457 <http://www.sciencedirect.com/science/article/pii/S002192901600018X>.

Rhee, J.S., Cannon, D.E., Frank, D.O., Kimbell, J.S., 2012. Role of virtual surgery in preoperative planning: assessing the individual components of functional nasal airway surgery. Arch. Facial Plastic. Surg. 14, 354–359.

Rhee, J.S., Pawar, S.S., Garcia, G.J., Kimbell, J.S., 2011. Toward personalized nasal surgery using computational fluid dynamics. Arch. Facial Plast. Surg. 13, 305–310.

Richardson, L., 1910. On the approximate arithmetical solution by finite differences of physical problems involving differential equations, with an application to the stresses in a masonry dam. Proc. Roy. Soc. London. Ser. A 83, 335–336.

Roache, P., 1994. Perspective: A method for uniform reporting of grid refinement studies. J. Fluids Eng. 116, 405–413.

Roithmann, R., Demeneghi, P., Faggiano, R., Cury, A., 2005. Effects of posture change on nasal patency. Braz. J. Otorhinolaryngol. 71 (4), 478–484.

Rygg, A., Longest, P., 2016. Absorption and clearance of pharmaceutical aerosols in the human nose: development of a cfd model. J. Aerosol Med. Pulmonary Drug Delivery 29, 416–431.

Schroeter, J.D., Garcia, G.J.M., Kimbell, J.S., 2011. Effects of surface smoothness on inertial particle deposition in human nasal models. J. Aerosol Sci. 42 (1), 52–63. URL <Go to ISI>://WOS:000286960200005..

Schroeter, J.D., Kimbell, J.S., Gross, E.A., Willson, G.A., Dorman, D.C., Tan, Y.-M., III, H. J.C., 2008. Application of physiological computational fluid dynamics models to predict interspecies nasal dosimetry of inhaled acrolein. Inhalation Toxicol. 20 (3), 227–243. https://doi.org/10.1080/08958370701864235, pMID: 18300045.

Se, M., Inthavong, K., Tu, J., 2009. Unsteady particle deposition in a human nasal cavity. In: Proceedings of the Seventh International Conference on CFD in the Minerals and Process Industries. CSIRO, pp. 1–6.

Shang, Y., Dong, J., Inthavong, K., Tu, J., 2015. Comparative numerical modeling of inhaled micron-sized particle deposition in human and rat nasal cavities. Inhalation Toxicol. 27, 694–705.

Shang, Y., Dong, J., Inthavong, K., Tu, J., 2017. Computational fluid dynamics analysis of wall shear stresses between human and rat nasal cavities. Eur. J. Mech.-B/Fluids 61, 160–169.

Shang, Y., Inthavong, K., Tu, J., 2015. Detailed micro-particle deposition patterns in the human nasal cavity influenced by the breathing zone. Comput. Fluids 114, 141–150 <http://www.sciencedirect.com/science/article/pii/S0045793015000638>.

Shang, Y., Inthavong, K., Tu, J., 2019. Development of a computational fluid dynamics model for mucociliary clearance in the nasal cavity. J. Biomech. 85, 74–83. https://doi.org/10.1016/j.jbiomech.2019.01.015.

Shi, H., Kleinstreuer, C., Zhang, Z., 2006. Laminar airflow and nanoparticle or vapor deposition in a human nasal cavity model. J. Biomech. Eng. 128 (5), 697–706.

Shi, H., Kleinstreuer, C., Zhang, Z., 2007. Modeling of inertial particle transport and deposition in human nasal cavities with wall roughness. J. Aerosol Sci. 38 (4), 398–419.

Subramaniam, R., Richardson, R., Morgan, K., Kimbell, J., Guilmette, R., 1998. Computational fluid dynamics simulations of inspiratory airflow in the human nose and nasopharynx. Inhalation Toxicol. 10 (2), 91–120. https://doi.org/10.1080/089583798197772.

Sullivan, C.D., Garcia, G., Frank-Ito, D., Kimbell, J.S., Rhee, J.S., 2014. Perception of better nasal patency correlates with increased mucosal cooling after surgery for nasal obstruction. Otolaryngol.-Head Neck Surg. 150, 139–147.

Taylor, D.J., Doorly, D.J., Schroter, R.C., 2006. Airflow in the human nasal cavity. J. Biomech. 39 (Supplement 1). S272–S272.

Taylor, D.J., Doorly, D.J., Schroter, R.C., 2009. Inflow boundary profile prescription for numerical simulation of nasal airflow. J. Roy. Soc. Interface 7, 515–527.

Tian, L., Inthavong, K., Liden, G., Shang, Y., Tu, J., 2016. Transport and deposition of welding fume agglomerates in a realistic human nasal airway. Ann. Occupat. Hygiene 60 (6), 731–747.

Tian, L., Shang, Y., Dong, J., Inthavong, K., Tu, J., 2017. Human nasal olfactory deposition of inhaled nanoparticles at low to moderate breathing rate. J. Aerosol Sci. 113, 189–200.

Tian, Z.F., Inthavong, K., Tu, J.Y., 2007. Deposition of inhaled wood dust in the nasal cavity. Inhalation Toxicol. 19 (14), 1155–1165.

Tong, X., Dong, J., Shang, Y., Inthavong, K., Tu, J., 2016. Effects of nasal drug delivery device and its orientation on sprayed particle deposition in a realistic human nasal cavity. Comput. Biol. Med. 77, 40–48.

Tu, J., Yeoh, G., Liu, C., 2012. Computational Fluid Dynamics: A Practical Approach. Elsevier Science <https://books.google.com.au/books?id=IQAc3z-2QYIC>.

Tucker, P., Pan, Z., 2000. A cartesian cut cell method for incompressible viscous flow. Appl. Math. Model. 24 (8), 591–606 <http://www.sciencedirect.com/science/article/pii/S0307904X00000056>.

Vanhille, D.L., Garcia, G.J.M., Asan, O., Borojeni, A.A.T., Frank-Ito, D.O., Kimbell, J.S., Pawar, S.S., Rhee, J.S., 2018. Virtual surgery for the nasal airway: a preliminary report on decision support and technology acceptancevirtual surgery for the nasal airwayvirtual surgery for the nasal airway. JAMA Facial Plastic Surg. 20 (1), 63–69. https://doi.org/10.1001/jamafacial.2017.1554.

Vinchurkar, S., Longest, P.W., 2008. Evaluation of hexahedral, prismatic and hybrid mesh styles for simulating respiratory aerosol dynamics. Comput. Fluids 37, 317–331.

Wang, D.Y., Lee, H.P., Gordon, B.R., 2012. Impacts of fluid dynamics simulation in study of nasal airflow physiology and pathophysiology in realistic human three-dimensional nose models. Clin. Exp. Otorhinolaryngol. 5, 181–187.

Wen, J., Inthavong, K., Tu, J., Wang, S., 2008. Numerical simulations for detailed airflow dynamics in a human nasal cavity. Respirat. Physiol. Neurobiol. 161 (2), 125–135 <http://www.sciencedirect.com/science/article/pii/S1569904808000189>.

Wittkopf, M., Wittkopf, J., Ries, W.R., 2008. The diagnosis and treatment of nasal valve collapse. Curr. Opin. Otolaryngol. Head Neck Surg. 16 (1), 10–13.

Wustrow, T.P., Kastenbauer, E., 1995. Surgery of the internal nasal valve. Facial Plastic surg. 11 (03), 213–227.

Xi, J., Kim, J., Si, X.A., 2016. Effects of nostril orientation on airflow dynamics, heat exchange, and particle depositions in human noses. Eur. J. Mech. B. Fluids 55, 215–228 <http://www.sciencedirect.com/science/article/pii/S0997754615300960>.

Xi, J., Zhang, Z., Si, X.A., Yang, J., Deng, W., 2016. Optimization of magnetophoretic-guided drug delivery to the olfactory region in a human nose model. Biomech. Model. Mechanobiol. 15 (4), 877–891. https://doi.org/10.1007/s10237-015-0730-9.

Yoo, S.-J., Ito, K., 2018. Numerical prediction of tissue dosimetry in respiratory tract using computer simulated person integrated with physiologically based pharmacokinetic–computational fluid dynamics hybrid analysis. Indoor Built Environ. 27 (7), 877–889. https://doi.org/10.1177/1420326X17694475.

Zhang, Y.J., 2001. A review of recent evaluation methods for image segmentation. In: Proceedings of the Sixth International Symposium on Signal Processing and its Applications (Cat. No. 01EX467), vol. 1, IEEE, pp. 148–151.

Zhao, K., Blacker, K., Luo, Y., Bryant, B., Jiang, J., 2011. Perceiving nasal patency through mucosal cooling rather than air temperature or nasal resistance. PLOS ONE 6 (10), 1–8. https://doi.org/10.1371/journal.pone.0024618.

Zhao, K., Craig, J.R., Cohen, N.A., Adappa, N.D., Khalili, S., Palmer, J.N., 2016. Sinus irrigations before and after surgery-visualization through computational fluid dynamics simulations. Laryngoscope 126, E90–E96.

Zhao, K., Jiang, J., 2014. What is normal nasal airflow? A computational study of 22 healthy adults. Int. Forum of Allergy Rhinol. 4 (6), 435–446 <https://onlinelibrary.wiley.com/doi/abs/10.1002/alr.21319>.

Zhao, K., Pribitkin, E.A., Cowart, B.J., Rosen, D., Scherer, P.W., Dalton, P., 2006. Numerical modeling of nasal obstruction and endoscopic surgical intervention: outcome to airflow and olfaction. Am. J. Rhinol. 20, 308–316.

Zhao, K., Scherer, P.W., Hajiloo, S.A., Dalton, P., 2004. Effect of anatomy on human nasal air flow and odorant transport patterns: implications for olfaction. Chem Senses 29, 365–379.

Zhu, J., Lee, H., Lim, K., Lee, S., Wang, d.Y., 2011. Evaluation and comparison of nasal airway flow patterns among three subjects from caucasian, chinese and indian ethnic groups using computational fluid dynamics simulation. Respir. Physiol. Neurobiol. 175, 62–69.

Zhu, J.H., Lee, H.P., Lim, K.M., Lee, S.J., San, L.T.L., Wang, D.Y., 2013. Inspirational airflow patterns in deviated noses: a numerical study. Comput. Methods Biomech. Biomed. Eng. 16 (12), 1298–1306. https://doi.org/10.1080/10255842.2012.670850, pMID: 22515677.

Zhu, J.H., Lim, K.M., Thong, K.T.M., Wang, D.Y., Lee, H.P., 2014. Assessment of airflow ventilation in human nasal cavity and maxillary sinus before and after targeted sinonasal surgery: a numerical case study. Respir. Physiol. Neurobiol. 194, 29–36.

Zubair, M., Abdullah, M., Ahmad, K., 2013a. Hybrid mesh for nasal airflow studies. Comput. Math. Methods Med. 2013 (Article ID 727362).

Zubair, M., Riazuddin, V., Abdullah, M., Ismail, R., Shuaib, I., Ahmad, K., 2013b. Computational fluid dynamics study of the effect of posture on airflow characteristics inside the nasal cavity. Asian Biomed. 7 (6), 835–840.